

# Oxide Ion Dynamics and Structure–Property Relationships in $A_3\text{OhTd}_2\text{O}_{7.5}$ Ionic Conductors (A = Ba, Sr; Oh = Y; Td = Ga, Zn)

Oliver J. Wagstaff, Maxim Avdeev, Stewart J. Clark, John S. O. Evans,\* and Ivana Radosavljevic Evans\*



Cite This: *Chem. Mater.* 2025, 37, 3492–3503



Read Online

ACCESS |



Metrics & More

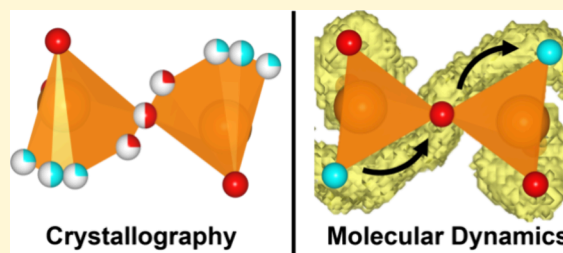


Article Recommendations



Supporting Information

**ABSTRACT:**  $A_3\text{OhTd}_2\text{O}_{7.5}$  materials (where Oh/Td = 6/4 coordinate metal ions) are a new class of ionic conductors, with potential applications in important technologies such as fuel cells. We report the first results of ab initio molecular dynamics simulations of oxide ion diffusion in  $\text{Sr}_3\text{YGa}_2\text{O}_{7.5}$  and identify a sinusoidal diffusion pathway along the *c*-axis direction enabled by the rotation and exchange of oxide ions between corner-sharing  $\text{GaO}_4$  tetrahedra. The highly anisotropic nature of oxide ion diffusion revealed by the simulations suggested that chemical modifications aimed at property improvements should focus on improving rotational flexibility within the tetrahedral layer. We hence used the simulations to inform subsequent development of materials in the series  $\text{Sr}_3\text{YGa}_{2-x}\text{Zn}_x\text{O}_{7.5-x/2}$  and  $\text{Ba}_{1.5}\text{Sr}_{1.5}\text{YGa}_{2-x}\text{Zn}_x\text{O}_{7.5-x/2}$  ( $0.05 \leq x \leq 0.20$ ). Structures were characterized with both ambient and variable temperature X-ray and neutron powder diffraction. All new materials adopt the room temperature *C2* and *P2/c* structures of the parent phases, albeit with significant static disorder in the oxygen substructure. The Ba-containing materials undergo a phase transition to space group *Cmcm* at around 700 °C, while  $\text{Sr}_3\text{YGa}_{1.8}\text{Zn}_{0.2}\text{O}_{7.4}$  transforms to space group *Ama2* at 850 °C. Impedance studies show that all samples exhibit mixed proton and oxide ion conductivity, with oxide ion conductivity dominating under dry atmospheres.  $\text{Sr}_3\text{YGa}_{1.8}\text{Zn}_{0.2}\text{O}_{7.4}$  exhibits the largest total conductivity of  $5.5 \times 10^{-4} \text{ S cm}^{-1}$ , an order of magnitude higher than unsubstituted  $\text{Sr}_3\text{YGa}_2\text{O}_{7.5}$ .



## 1. INTRODUCTION

Oxide ion conductors are important functional materials used as electrolytes in solid oxide fuel cells (SOFCs), as oxygen separation membranes or for partial oxidation of fossil fuels during reforming.<sup>1,2</sup> SOFCs are among the most promising alternative technologies to traditional energy conversion, offering high efficiencies (up to 80%) and fuel flexibility.<sup>3</sup> Widespread usage of these devices is limited by the high temperatures (700–1000 °C) at which conventional electrolyte materials (yttria-stabilized zirconia and gadolinia-doped ceria) have sufficient ionic conductivity to be used in practical devices.<sup>4,5</sup> Materials which conduct at intermediate temperatures (450–600 °C) are required to further encourage the adoption of SOFC technology. The identification of such materials depends on a greater understanding of the relationships between composition, structure, and ionic conduction pathways.

Among the compounds that have been identified as promising oxide ion conductors, there are several families with tetrahedral disorder, or structurally flexible tetrahedra, as a common feature.<sup>6</sup> Examples include  $\text{La}_2\text{Mo}_2\text{O}_9$ , melilite, brownmillerite,  $\text{Bi}_{1-x}\text{V}_x\text{O}_{1.5+\delta}$  and  $\text{Ba}_3\text{NbMoO}_{8.5}$ -derived compounds.<sup>7–14</sup> In these and related materials migrating oxide ions (interstitial or vacancy) are stabilized via temporary association with tetrahedral units, reducing the energy barrier to long-range ionic diffusion.

$A_3\text{OhTd}_2\text{O}_{7.5}$  materials (A = 2<sup>+</sup> cation, Oh = 6-coordinate 3<sup>+</sup> cation, Td = tetrahedral 3<sup>+</sup> cation) have recently been identified as a promising family of oxygen-deficient perovskite derivatives.<sup>15–17</sup> The basic structure is a 12-fold supercell of cubic perovskite  $\text{ABO}_3$  ( $2a_p \times \sqrt{2}a_p \times 3\sqrt{2}a_p$ ) with 17% of the available oxygen sites vacant. A sufficiently large difference in ionic radius between the two B-site cations results in the ordering of the  $\text{BO}_x$  polyhedra into infinite  $[(\text{TdO}_4)(\text{OhO}_6)]_2$  slabs separated by layers of  $\text{Td}_2\text{O}_7$  corner-sharing tetrahedra (Figure 1). The  $\text{Td}_2\text{O}_7$  subunits are connected by a bridging oxygen ( $\text{O}_b$ ) and contain two terminal oxygen sites ( $\text{O}_t$ , Figure 1). Terminal oxygens are of particular interest because similar sites in melilite-type  $\text{La}_{1.54}\text{Sr}_{0.46}\text{Ga}_3\text{O}_{7.27}$  and  $\text{Ca}_2\text{Ga}_2\text{GeO}_7$  impart significant structural freedom, enabling the stabilization of migrating oxide ions.<sup>9,18,19</sup> As such these sites are an indicator of potential ionic conductivity.

Ionic conductivity has recently been demonstrated in  $\text{Ba}_3\text{YGa}_2\text{O}_{7.5}$  and several closely related materials.<sup>15,16</sup>  $\text{Ba}_3\text{YGa}_2\text{O}_{7.5}$  adopts a monoclinic *P2/c* structure at room

Received: February 21, 2025

Revised: April 8, 2025

Accepted: April 8, 2025

Published: April 16, 2025



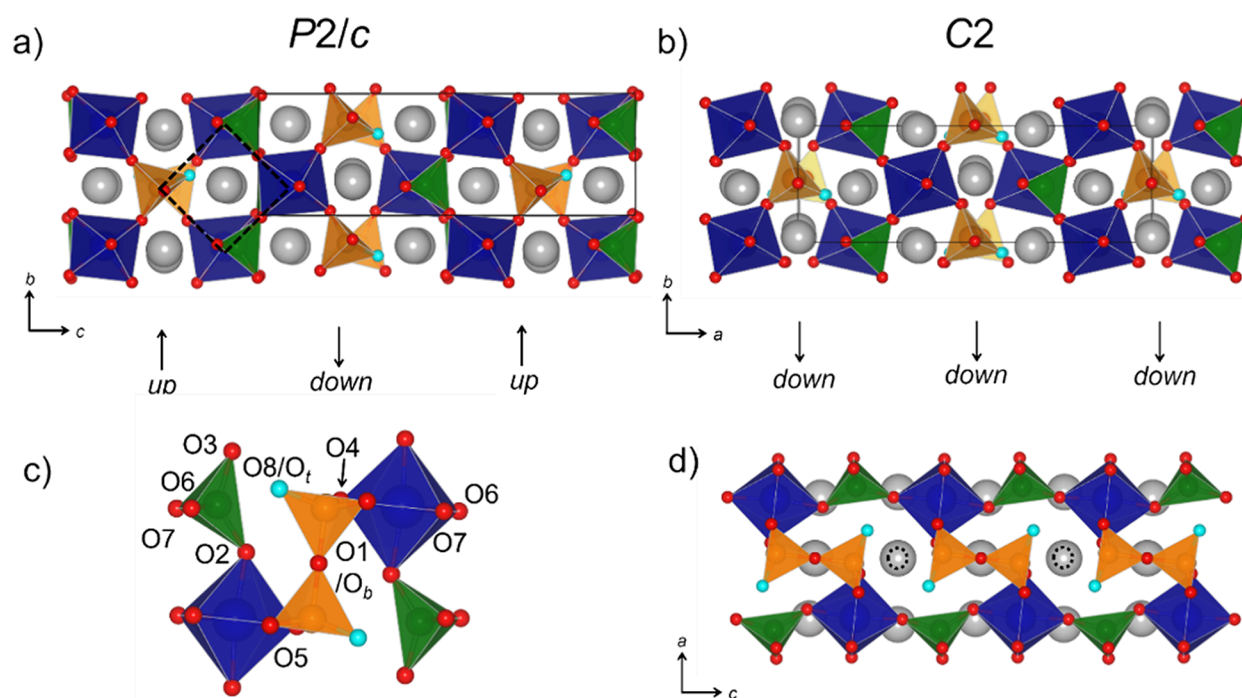


**Figure 1.** (a)  $P2/c$  and (b)  $C2$   $A_3\text{OhTd}_2\text{O}_{7.5}$  structures with relative orientations of  $\text{Td}_2\text{O}_7$  units shown with arrows. The underlying cubic perovskite subcell is indicated with a dashed box in Figure 1a. Oxygen atom labels are given in (c) with the terminal O8 ( $\text{O}_t$  in text) in cyan. The bridging O1 ( $\text{O}_b$  in text) is also shown. The ordered arrangement of oxygen vacancies is shown in (d) with unoccupied sites indicated by dashed circles.

temperature (Figure 1a), but undergoes a reversible first order phase transition around 760 °C. The high temperature  $P2_1/a$  structure contains alternating  $\text{Ga}_2\text{O}_7$  chains displaced by half a unit cell, rather than the disorder ( $-\text{O}_{0.5}-\text{Ga}-\text{O}_{0.5}-$ ) previously suggested for  $\text{Ba}_3\text{MAl}_2\text{O}_{7.5}$  compounds.<sup>20,21</sup> Several materials obtained by aliovalent substitution in  $\text{Ba}_3\text{YGa}_2\text{O}_{7.5}$  ( $\text{Ba}^{2+} \leftrightarrow \text{La}^{3+}$ ,  $\text{Ga}^{3+} \leftrightarrow \text{Ti}^{4+}$ ,  $\text{Ge}^{4+}$ ,  $\text{Zn}^{2+}$ , and  $\text{Y}^{3+} \leftrightarrow \text{Zr}^{4+}$ ) show the same  $P2/c \leftrightarrow P2_1/a$  phase transition at approximately the same temperature.<sup>16</sup> These compounds show an increase of up to an order of magnitude in total conductivity and displayed different behaviors, with pure oxide ion conductivity observed for  $\text{La}^{3+}$  and  $\text{Ti}^{4+}$  substituted materials, and mixed oxide ion and proton conductivity observed for the  $\text{Zn}^{2+}$  containing compounds up to 800 °C.

Isovalent substitution of  $\text{Ba}^{2+}$  for  $\text{Sr}^{2+}$  in the series  $\text{Ba}_{3-x}\text{Sr}_x\text{YGa}_2\text{O}_{7.5}$  ( $0.0 \leq x \leq 3.0$ ) further broadened the structural and conductivity landscape of  $A_3\text{OhTd}_2\text{O}_{7.5}$  materials.<sup>16</sup> Ba-rich materials ( $x \leq 0.6$ ) adopt the  $P2/c$  structure at room temperature, while Sr rich phases ( $x \geq 2.4$ ) adopt a related monoclinic structure with space group  $C2$  (Figure 1b).<sup>22</sup> The reduction in A-site ionic radius results in the reorientation of the  $\text{Ga}_2\text{O}_7$  (pyrogallate) groups, producing an overall C-centered structure. The Sr-rich compounds do not undergo phase transitions below 1000 °C. The structures of mixed Ba/Sr compounds ( $0.6 < x < 2.4$ ) could not be completely described by either monoclinic model, appearing orthorhombic at room temperature. HAADF-STEM imaging identified that  $\text{Sr}^{2+}$  partially segregates to lower-coordination A-sites, introducing stacking faults that result in an average orthorhombic cell. These stacking faults were found to be most evident for the  $x = 1.5$  composition. The mixed A-site compounds adopt a disordered  $Cmcm$  structure when heated, although local ordering of  $\text{Ga}_2\text{O}_7$  subunits was suspected. Increasing the Sr-content resulted in lower total conductivity

( $\sim 6 \times 10^{-6} \text{ S cm}^{-1}$  for  $\text{Sr}_3\text{YGa}_2\text{O}_{7.5}$ ) and a reduced proton component. Despite this, the Sr-rich materials are a potentially interesting route for further modifications because, unlike the Ba-rich materials, they are not moisture-sensitive and are stable under atmospheric conditions.

To date there have been no computational studies on these materials. These are essential to understand the role of the  $\text{Td}_2\text{O}_7$  subunits and terminal oxygen sites in ionic diffusion, and could enable systematic improvements in properties. In this paper we report ab initio molecular dynamics (AIMD) simulations of oxide ion diffusion in  $A_3\text{OhTd}_2\text{O}_{7.5}$  materials. Continuous ionic diffusion pathways were observed arising from oxygen exchange along the chains of  $\text{Td}_2\text{O}_7$  groups (parallel to the  $c$ -axis of  $\text{Sr}_3\text{YGa}_2\text{O}_{7.5}$ , Figure 1d), indicating anisotropic ionic diffusion. Analysis of the AIMD simulations suggested that a targeted modification of the tetrahedral site could result in significantly increased ionic conductivity. Accordingly, we prepared two series of new materials:  $\text{Sr}_3\text{YGa}_{2-x}\text{Zn}_x\text{O}_{7.5-x/2}$  and  $\text{Ba}_{1.5}\text{Sr}_{1.5}\text{YGa}_{2-x}\text{Zn}_x\text{O}_{7.5-x/2}$  ( $x = 0.0, 0.05, 0.10, \text{ and } 0.20$ ). Across the two series we observe changes in conductivity and structural phase transitions dependent on Zn-content. We report the room- and high-temperature structures determined using variable-temperature X-ray and neutron powder diffraction, as well as conductivities measured by impedance spectroscopy, demonstrating variations in oxide and proton contribution with varying Zn-content. Finally, we correlate the changes in structure and conductivity with the ion dynamics revealed by the computational study.

## 2. EXPERIMENTAL SECTION

**2.1. Synthesis.** Polycrystalline samples of  $\text{Sr}_3\text{YGa}_2\text{O}_{7.5}$  and  $\text{Ba}_{1.5}\text{Sr}_{1.5}\text{YGa}_2\text{O}_7$  were prepared from stoichiometric ratios of  $\text{SrCO}_3$  (Sigma-Aldrich,  $\geq 99.9\%$ ),  $\text{Y}_2\text{O}_3$  (Sigma-Aldrich, 99.99%),

$\text{Ga}_2\text{O}_3$  (Sigma-Aldrich,  $\geq 99.99\%$ ) and  $\text{BaCO}_3$  (Sigma-Aldrich,  $\geq 99\%$ ). Reagents were mixed and ground together in ethanol, then heated in alumina crucibles for up to 100 h at 1200–1300 °C with a heating and cooling rate of 5 °C  $\text{min}^{-1}$ . Intermediate regrinding and pelleting were carried out until powder X-ray diffraction patterns of each sample were constant. The substituted series  $\text{Sr}_3\text{YGa}_{2-x}\text{Zn}_x\text{O}_{7.5-x/2}$  ( $x = 0.05, 0.10, 0.20, 0.30, 0.40$ ) and  $\text{Ba}_{1.5}\text{Sr}_{1.5}\text{YGa}_{2-x}\text{Zn}_x\text{O}_{7.5-x/2}$  ( $x = 0.05, 0.10, 0.20$ ) were made by the same method using additional stoichiometric ZnO (Sigma-Aldrich,  $\geq 99.9\%$ ). All phases formed as white powders and could be prepared on a 10 g scale.

**2.2. X-ray Diffraction.** Ambient X-ray diffraction measurements were collected on a Bruker D8 Advance Powder Diffractometer in Bragg–Brentano geometry using Cu  $K\alpha$  radiation and a Lynx-eye detector. Measurements for final Rietveld analysis were collected with a  $2\theta$  range of  $10 \leq 2\theta \leq 120^\circ$ . Analysis was carried via Rietveld refinement implemented in the TOPAS Academic software.<sup>23–25</sup>

Variable temperature X-ray diffraction patterns were recorded with an Anton Parr HTK1200 Furnace attachment. X-ray diffraction patterns were collected on heating and cooling at 20 °C intervals between 25 and 1000 °C over a  $2\theta$  range of  $10 \leq 2\theta \leq 90^\circ$ . Collection times were 30 min at each temperature. Furnace temperatures were calibrated using an external alumina standard. The resulting diffraction patterns were analyzed by sequential Rietveld fitting.

**2.3. Neutron Powder Diffraction.** Approximately 4 g of each sample was packed into 6 mm cylindrical vanadium cans. High-resolution time-of-flight (TOF) powder diffraction patterns were collected on the High Resolution Powder Diffraction (HRPD) instrument at the ISIS Neutron and Muon Source (Rutherford Appleton Laboratory). A 3 h measurement was collected at room temperature for each sample. For  $\text{Ba}_{1.5}\text{Sr}_{1.5}\text{YGa}_2\text{O}_{7.5}$  and  $\text{Ba}_{1.5}\text{Sr}_{1.5}\text{YGa}_{1.8}\text{Zn}_{0.2}\text{O}_{7.4}$  an additional series of 14 min measurements was collected on heating at 20 °C intervals over a temperature range of 30–1000 °C using the ISIS ‘Risø’ furnace. Data were processed using routines within Mantid Software and analyzed using TOPAS Academic. Rietveld fitting was carried out for the two highest resolution data banks (banks 1 and 2;  $2\theta = 168.567^\circ$  and  $90.2481^\circ$  respectively) giving an approximate  $d$ -spacing range of 0.65–3.90 Å.<sup>26</sup>

Diffraction patterns were also collected on 6 g samples of  $\text{Sr}_3\text{YGa}_{1.9}\text{Zn}_{0.1}\text{O}_{7.4}$  and  $\text{Sr}_3\text{YGa}_{1.8}\text{Zn}_{0.2}\text{O}_{7.4}$  packed into 9 mm vanadium cans on the high-resolution diffractometer ECHIDNA at ANSTO. Patterns were collected at room temperature and 850 °C.<sup>27</sup>

**2.4. Impedance Spectroscopy.** Samples for impedance spectroscopy were pressed into 10 mm pellets. These were sintered to achieve the highest possible density, as summarized in Table S1. Platinum ink (Metalor) was applied to the faces of each pellet before mounting on a Probotat A-6 cell placed inside a vertically oriented tube furnace. Platinum wire electrodes were attached to each face and set by heating to 1000 °C for 30 min. Impedance measurements were collected at  $\sim 20$  °C intervals on heating and cooling between 20 and 1000 °C at 2 °C  $\text{min}^{-1}$  using a Solartron 1260 frequency response analyzer. Applied frequencies and voltages of  $10^{-1}$ – $10^7$  Hz and 500 mV, respectively, were used. The results were analyzed using the ZView/ZPlot Software (Scribner Associates). Further measurements were carried out under dry or wet flowing  $\text{N}_2$  ( $p_{\text{H}_2\text{O}} \sim 0.02$  atm), with multiple cycles of heating and cooling to ensure equilibrium had been achieved.

**2.5. Ab Initio Molecular Dynamics (AIMD).** Density functional theory (DFT) calculations were carried out using plane wave pseudopotentials in the CASTEP code on a single cell of  $\text{Sr}_3\text{YGa}_2\text{O}_{7.5}$ .<sup>28</sup> The calculations used the generalized gradient approximation (GGA) Perdew–Burke–Ernzerhof for solids (PBEsol) exchange–correlation functional and a  $3 \times 1 \times 2$  Monkhorst–Pack grid for  $k$ -point sampling. AIMD calculations were performed in an NVT ensemble controlled with a Nosé–Hoover thermostat using a geometry-optimized cell as the starting model. A time step of 1 fs was used, and simulations were carried out for a total of 200 ps at 3 temperatures, 727, 1000, and 1273 °C. MDANSE code and Python scripts were used for data analysis.<sup>29</sup> The space visited by the atoms

was visualized in the form of cloud plots using isosurfaces in VESTA.<sup>30</sup>

**2.6. Thermogravimetric Analysis.** Mass changes on heating and cooling cycles were measured using a PerkinElmer TGA 8000 instrument. Powdered samples of  $\text{Sr}_3\text{YGa}_{1.8}\text{Zn}_{0.2}\text{O}_{7.4}$  and  $\text{Ba}_{1.5}\text{Sr}_{1.5}\text{YGa}_{1.8}\text{Zn}_{0.2}\text{O}_{7.4}$  were heated and cooled between 30 and 1000 °C at a rate of 10 °C  $\text{min}^{-1}$  under flowing air.

### 3. RESULTS AND DISCUSSION

**3.1. Oxide Ion Dynamics Investigated by Ab Initio Molecular Dynamics.** The cloud plots showing the regions visited by atoms over the course of the 1000 °C simulation (Figure 2) are representative of those observed across all

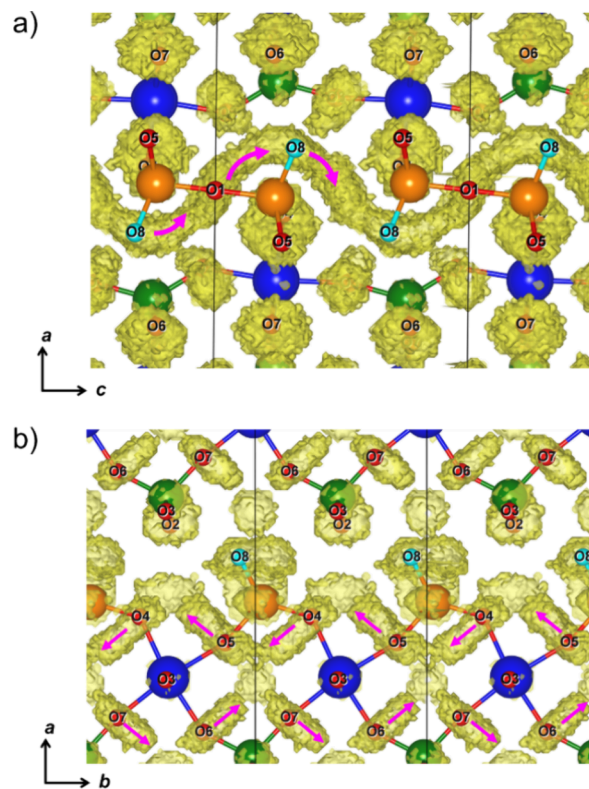


**Figure 2.** Representative cloud plots showing the space visited by oxide ions during AIMD simulations of  $\text{Sr}_3\text{YGa}_2\text{O}_{7.5}$  at 1000 °C. (a) The sinusoidal diffusion pathway between  $\text{Ga}_2\text{O}_7$  units (pink arrows show O<sub>1</sub>–O<sub>8</sub> hopping steps); (b) localized polyhedral rotations that drive the symmetry-raising phase transition (shown with pink arrows).

simulations. The continuous volume depicted in yellow indicates a sinusoidal oxide ion diffusion pathway along the  $c$ -direction involving the bridging O<sub>b</sub> and terminal O<sub>t</sub> atoms (Figure 2a) of the pyrogallate units. All other atoms remain effectively localized, vibrating around their starting positions with no long-range diffusion.

Inspection of the individual trajectories of selected oxygen atoms (Figure 3) shows that the cloud plots represent an individual  $\text{GaO}_4$  tetrahedron rotating so that an initial O<sub>t</sub> occupies the vacant site between two  $\text{Ga}_2\text{O}_7$  units. The same event breaks the existing Ga–O<sub>b</sub>–Ga dimer as the O<sub>b</sub> moves to replace the migrating O<sub>t</sub>. This creates a new  $\text{Ga}_2\text{O}_7$  subunit as a second  $\text{GaO}_4$  tetrahedron tilts to stabilize the forming dimer. The correlated nature of these movements for a given  $\text{Ga}_2\text{O}_7$  chain can be seen in Figure 3, where shaded regions

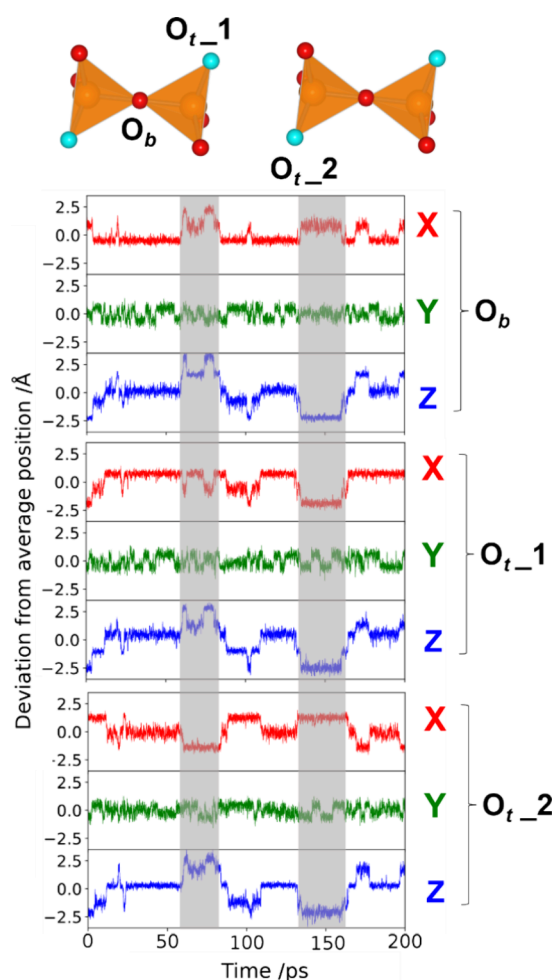


**Figure 3.** Coordinates of three atoms involved in the diffusion pathway along  $(0, 0, z)$  during the 1000 °C simulation. Shaded regions enclose examples of concerted O atom jumps.

indicate that diffusion events occur in the  $ac$  plane correlated to within a few picoseconds.

The volume visited by all O atoms increases with temperature, as expected (Figure S1a); however, the sinusoidal pathway remains the same and no other diffusion pathways are observed. The statistical distribution of the ions within the trajectory, shown in Figure S1b, displays saddle-point-like behavior. The number of  $O_t$  and  $O_b$  jumps (defining a jump as a deviation in position by 1 Å for more than 2 ps, or 2000 simulation steps) increases with temperature (Figure 4a), as anticipated. The increased oxide-ion motion with increasing temperature is also manifested in the mean square displacement (MSD) curves (Figure S2). The activation energy for oxide ion diffusion calculated from the diffusion coefficients at the three simulated temperatures (Figure 4b) is 0.31(8) eV, lower than the experimentally determined value (1.086(1) eV) from impedance measurements.<sup>16</sup> Similar differences between activation energies obtained from methods that probe atomic-scale dynamics (AIMD or NMR experiments) and macroscopic property measurements (impedance spectroscopy) are commonly found for ionic conductors.<sup>13,19,31–35</sup> The latter types of measurement are affected by factors such as particle morphology, sample porosity and grain boundaries, and typically give higher activation energy values. The probability density distribution of O atoms based on the AIMD

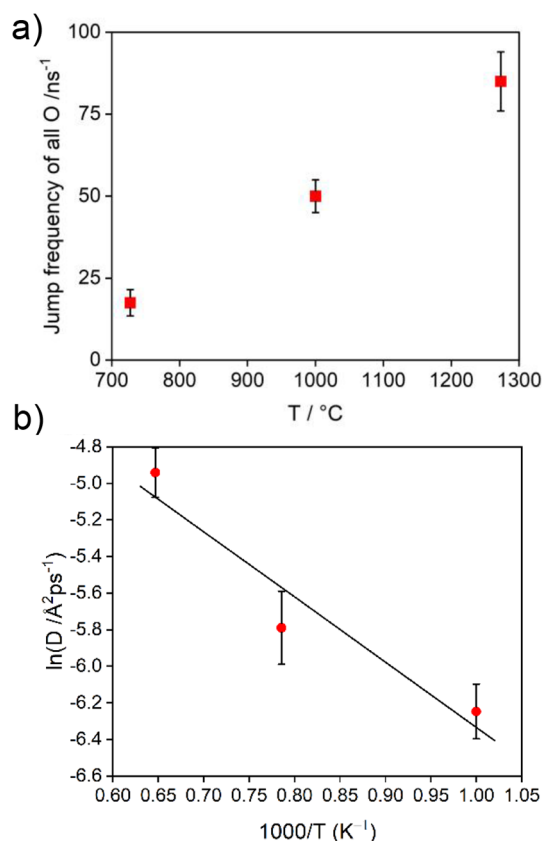


**Figure 4.** (a) O site hopping frequency at the three simulated temperatures. (b) Arrhenius plot of diffusion coefficients for all oxygen atoms calculated from the gradients of the total MSD curves.

simulations was also used to estimate one-particle potential in the framework of Boltzmann statistics.<sup>36</sup> The resulting local activation barriers are consistent with the long-range diffusion activation energy. The MSD curves calculated along each Cartesian direction reveals a high degree of anisotropy of oxide ion diffusion in  $\text{Sr}_3\text{YGa}_2\text{O}_{7.5}$ , with the  $c$ -axis being the most favorable direction (Figure S3). This is consistent with the crystal structure, as discussed in Section 3.3.

Additional localized dynamics in  $\text{Sr}_3\text{YGa}_2\text{O}_{7.5}$  can be inferred from the trajectories of the nondiffusing O atoms ( $\text{O}_2$ – $\text{O}_7$ , Figures S4–S6). Atoms  $\text{O}_2$  and  $\text{O}_3$  in the  $[(\text{GaO}_4)(\text{YO}_6)]_2$  slabs only undergo small thermal fluctuations around their equilibrium position. The remaining O atoms connect the mixed Oh/Td layers to the  $\text{Ga}_2\text{O}_7$  units. The atomic trajectories clearly show polyhedral rotations in the  $ab$  plane at a rate approaching the picosecond time scale without long-range diffusion (Figure 2b, with an animated version available as SI). At 727 °C, these rotations appear correlated across the mixed octahedral layers such that all metal–oxygen polyhedra tend to tilt either all ‘left’ or all ‘right’ (Figure 5). At higher temperatures, the rate of these rotations significantly increases and the cooperativity between separate layers is lost.  $\text{A}_3\text{OhTd}_2\text{O}_{7.5}$  materials are known to undergo symmetry-raising transitions upon heating, which are reproduced in our simulations as the loss of directional polyhedral tilting at 1000 and 1273 °C.<sup>15,37</sup> A variety of similar phase transitions have been observed in MD studies of perovskites.<sup>38–41</sup>

**3.2. Synthesis of Zn-Containing Materials.** The sinusoidal oxide ion diffusion pathway identified from the AIMD simulations suggested that tailored substitution on the Td

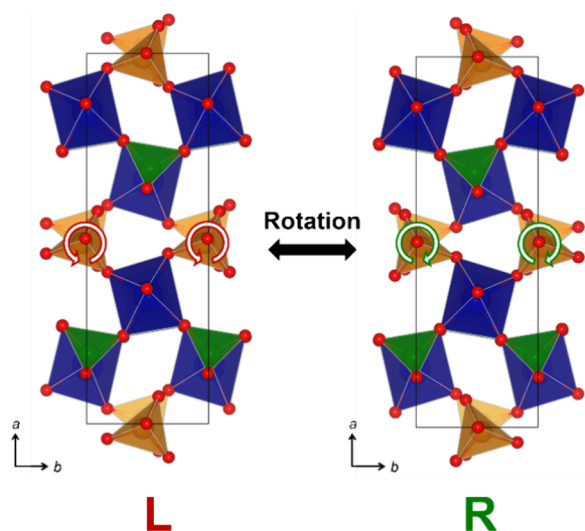


**Figure 5.** ‘left’ (L) and ‘right’ (R) orientations of polyhedral tilts in the *ab* plane. Rotation between the two takes place on the order of a few picoseconds. Sr atoms are omitted for clarity.

(=Ga) site should increase conductivity. Synthesis of eight compounds in the solid solution series  $\text{Sr}_3\text{YGa}_{2-x}\text{Zn}_x\text{O}_{7.5-x/2}$  ( $0.0 \leq x \leq 0.40$ ) and  $\text{Ba}_{1.5}\text{Sr}_{1.5}\text{YGa}_{2-x}\text{Zn}_x\text{O}_{7.5-x-2}$  ( $0.0 \leq x \leq 0.20$ ) was therefore attempted. PXRD patterns of  $\text{Sr}_3\text{YGa}_{2-x}\text{Zn}_x\text{O}_{7.5-x/2}$  samples for  $x = 0.30$  and  $0.40$  contained impurity peaks that increased in intensity with Zn-content, suggesting a solid solution limit of  $x = 0.2$  (Figure S7).

### 3.3. Ambient Structures of Zn-Containing Materials.

The structures of  $\text{Sr}_3\text{YGa}_2\text{O}_{7.5}$  and  $\text{Ba}_{1.5}\text{Sr}_{1.5}\text{YGa}_2\text{O}_{7.5}$  have been described in detail previously; here we only highlight the key structural features needed for further discussion.<sup>16</sup>  $\text{Sr}_3\text{YGa}_2\text{O}_{7.5}$  adopts a monoclinic *C2* structure (Figure 1b) with  $\beta \approx 90.6^\circ$ , while  $\text{Ba}_{1.5}\text{Sr}_{1.5}\text{YGa}_2\text{O}_{7.5}$  appears metrically orthorhombic due to the intergrowth of Ba- and Sr-rich regions, but has an overall primitive structure, which we represent here using a monoclinic *P2/c* model with  $\beta \approx 90^\circ$ . These two structural models provide good fits to laboratory X-ray diffraction patterns of  $\text{Sr}_3\text{YGa}_2\text{O}_{7.5}$  and  $\text{Ba}_{1.5}\text{Sr}_{1.5}\text{YGa}_2\text{O}_{7.5}$  (Figures S8a and S12a, respectively). The PXRD patterns for the  $\text{Sr}_3\text{YGa}_{1-x}\text{Zn}_x\text{O}_{7.5-x/2}$  ( $0.05 \leq x \leq 0.20$ ) compositions were all fitted with the same *C2* model (Figures 6, 7 and S8b–d). This gave weighted R-factors ( $R_{\text{wp}}$ ) of 3.25, 3.13, and 3.54% for  $x = 0.05$ , 0.10, and 0.20, respectively (Figure 7a). The monoclinic angle  $\beta$  decreases linearly with  $x$  (Figure 7b), supporting successful incorporation of Zn. For  $x = 0.20$  the angle is sufficiently close to  $90^\circ$  ( $= 90.1544(9)^\circ$ ) that peaks characteristic of the monoclinic distortion (e.g., the 312 and 312 reflections at  $2\theta \sim 31.5^\circ$ ) overlap. The *a* and *b* axes increase linearly as Zn-content increases, while the *c* axis decreases (Figure 7b).

The PXRD patterns for the  $\text{Ba}_{1.5}\text{Sr}_{1.5}\text{YGa}_{2-x}\text{Zn}_x\text{O}_{7.5-x/2}$  series were fitted with the *P2/c* model, which gave good agreement factors of 5.40, 4.30, and 3.74% (Figure S12b–d) and  $\beta$  angles very close to  $90^\circ$  (Table 1). The *a*- and *c*- (corresponding to the *c*- and *a*-axes in the *C2* setting) cell lengths, respectively, decrease and increase linearly with Zn-content (Figure S9). There are a few calculated weak peaks with zero observed intensity (e.g., at  $2\theta \approx 27.3^\circ$  and  $33.7^\circ$ ) in the Zn-substituted  $\text{Ba}_{1.5}\text{Sr}_{1.5}\text{YGa}_2\text{O}_{7.5}$  compositions. This indicates that the local structure is similar to the unsubstituted material, with the presence of local C-centering in an overall

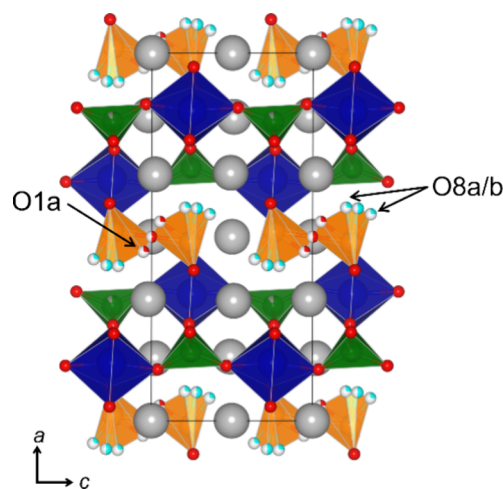


**Figure 6.** Final room temperature model for  $\text{Sr}_3\text{YGa}_{1.8}\text{Zn}_{0.2}\text{O}_{7.4}$ . Gray =  $\text{Sr}^{2+}$ , green/yellow =  $\text{Ga}^{3+}$ ,  $\text{Zn}^{2+}$ , blue =  $\text{Y}^{3+}$  and red/cyan =  $\text{O}^{2-}$ . The disordered O1a, O8a, and O8b sites are indicated with arrows.

primitive structure, therefore substitution at the Td site does not impact the formation of Sr-rich regions.

The final refinements for each series used a single isotropic temperature factor ( $B_{\text{iso}}$ ) for each atom type. For  $\text{Sr}_3\text{YGa}_{1.8}\text{Zn}_{0.2}\text{O}_{7.4}$  and  $\text{Ba}_{1.5}\text{Sr}_{1.5}\text{YGa}_{1.8}\text{Zn}_{0.2}\text{O}_{7.4}$  the  $B_{\text{iso}}(\text{O})$  value was larger than expected at room temperature, which is often indicative of disorder.<sup>42,43</sup> Samples of  $\text{Sr}_3\text{YGa}_{1.9}\text{Zn}_{0.1}\text{O}_{7.45}$ ,  $\text{Sr}_3\text{YGa}_{1.8}\text{Zn}_{0.2}\text{O}_{7.4}$ ,  $\text{Ba}_{1.5}\text{Sr}_{1.5}\text{YGa}_2\text{O}_{7.5}$ ,  $\text{Ba}_{1.5}\text{Sr}_{1.5}\text{YGa}_{1.9}\text{Zn}_{0.1}\text{O}_{7.45}$ , and  $\text{Ba}_{1.5}\text{Sr}_{1.5}\text{YGa}_{1.8}\text{Zn}_{0.2}\text{O}_{7.4}$  were selected for neutron diffraction studies to further investigate the oxygen atom arrangement.

For  $\text{Sr}_3\text{YGa}_{1.9}\text{Zn}_{0.1}\text{O}_{7.45}$  laboratory X-ray data and two constant wavelength neutron data sets from ECHIDNA ( $\lambda \sim 1.622$  and  $2.4395$  Å) were simultaneously fitted with the *C2* structural model. For  $\text{Sr}_3\text{YGa}_{1.8}\text{Zn}_{0.2}\text{O}_{7.4}$  the two highest resolution banks of neutron diffraction data from HRPD were used. In both cases large temperature factors at the  $\text{O}_b$  and  $\text{O}_t$  sites indicated disorder, which was modeled using split sites. The final model consists of 50% occupied  $\text{O}_b$  (O1) and  $\text{O}_t$  (O8) sites, a 25% occupied O1a site near the  $2a$  special position and 25% occupied O8a and O8b sites. Figure 6 shows the structure obtained for  $\text{Sr}_3\text{YGa}_{1.8}\text{Zn}_{0.2}\text{O}_{7.4}$ . The final fits (Figures S10 and S11 for  $x = 0.1$  and  $0.2$ , respectively) with this model gave a  $R_{\text{wp}}$  of 3.25 and 4.04%, as well as more sensible temperature factors (Table S2). Significantly, the site disorder obtained from diffraction data closely resembles the shape of the calculated oxygen diffusion pathway in the AIMD simulations, providing further evidence that this is indeed the mechanism by which long-range oxide ion diffusion occurs in these materials.

For  $\text{Ba}_{1.5}\text{Sr}_{1.5}\text{YGa}_2\text{O}_{7.5}$ ,  $\text{Ba}_{1.5}\text{Sr}_{1.5}\text{YGa}_{1.9}\text{Zn}_{0.1}\text{O}_{7.45}$ , and  $\text{Ba}_{1.5}\text{Sr}_{1.5}\text{YGa}_{1.8}\text{Zn}_{0.2}\text{O}_{7.4}$  neutron powder diffraction data were fitted with the *P2/c* model. Large  $B_{\text{iso}}$  values were observed at all oxygen sites associated with the pyrogallate units. These materials contain Ba- and Sr-rich regions and it is likely that the tetrahedra in the Sr-rich regions are able to tilt in a manner similar to that in the *C2* model (Figure 8a) to satisfy the bond valence of the smaller  $\text{Sr}^{2+}$  cations. In Ba-rich regions primitive-type local tilting occurs (Figure 8b). Substantial improvements in both  $B_{\text{iso}}$  and  $R_{\text{wp}}$  values were achieved by refining three additional partially occupied oxygen sites to represent these local distortions. Each of the new sites (O4a,

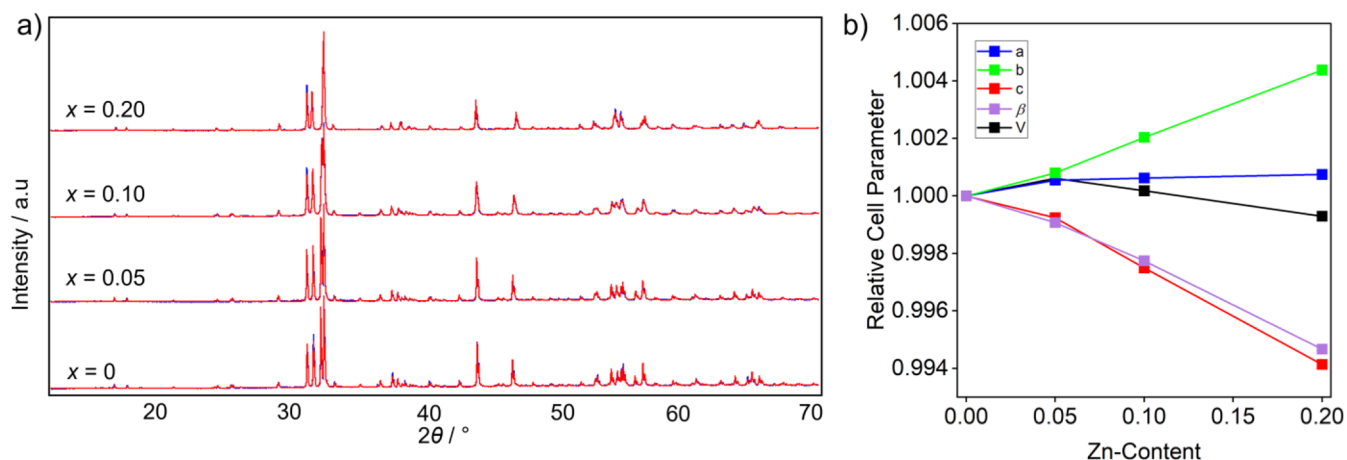


**Figure 7.** (a) Rietveld fits of powder X-ray diffraction patterns of the  $\text{Sr}_3\text{YGa}_{2-x}\text{Zn}_x\text{O}_{7.5-x/2}$  series and (b) unit cell parameter evolution with Zn-content. In figure (b), uncertainties are smaller than the plotted points.

**Table 1.**  $\text{Sr}_3\text{YGa}_{2-x}\text{Zn}_x\text{O}_{7.5-x/2}$  and  $\text{Ba}_{1.5}\text{Sr}_{1.5}\text{YGa}_{2-x}\text{Zn}_x\text{O}_{7.5-x/2}$  Unit-Cell Parameters

Zn content	$a/\text{Å}$	$b/\text{Å}$	$c/\text{Å}$	$\beta/^\circ$	$V/\text{Å}^3$
<b><math>\text{Sr}_3\text{YGa}_{2-x}\text{Zn}_x\text{O}_{7.5-x/2}</math></b>					
0	17.7122(2)	5.80964(5)	7.81300(7)	90.6377(6)	803.92(2)
0.05	17.7219(2)	5.81470(7)	7.80895(8)	90.5537(6)	804.41(2)
0.1	17.7232(3)	5.8215(1)	7.7934(2)	90.4328(9)	804.06(3)
0.2	17.72544(3)	5.83508(8)	7.7672(1)	90.1544(8)	803.35(2)
<b><math>\text{Ba}_{1.5}\text{Sr}_{1.5}\text{YGa}_{2-x}\text{Zn}_x\text{O}_{7.5-x/2}</math></b>					
0	7.8727(2)	5.9186(2)	18.0728(5)	90.012(7)	842.12(4)
0.05	7.8690(2)	5.9164(2)	18.0671(4)	90.020(5)	841.12(3)
0.1	7.8605(4)	5.9172(3)	18.1055(9)	90.046(4)	842.86(4)
0.2	7.8498(2)	5.9166(2)	18.1294(4)	90.006(7)	842.07(4)

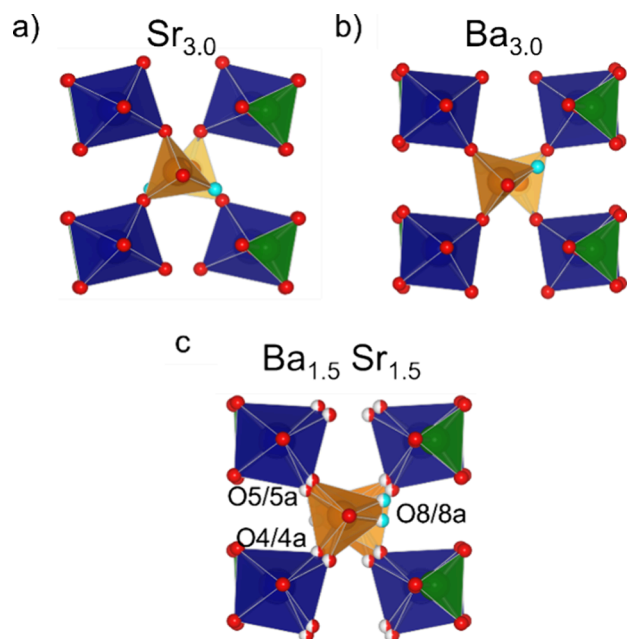


**Figure 8.** Tilting of the  $\text{OhO}_6$  and  $\text{TdO}_4$  polyhedra in  $\text{A}_3\text{OhTdO}_{7.5}$  compounds for (a) the  $C2$  structure and (b) the  $P2/c$  structure. (c) Positions refined from neutron data for  $\text{Ba}_{1.5}\text{Sr}_{1.5}\text{YGa}_2\text{O}_{7.5}$  indicating the presence of  $C2$ -type defect layers. A cations are omitted for clarity.

$\text{Sa}$ , and  $8a$ ) refined to a position on a theoretical rotation from  $P2/c$  to  $C2$ -like tilting, indicating this is a reasonable description of the average structure (Figure 8c). A further

improvement was obtained for the  $x = 0.1$  and  $0.2$  compounds by including the same static disorder at the  $\text{O}_b$  site found for the Sr-only materials. This model provides good fits to both X-ray and neutron diffraction data. Final fits and models are shown and described in Figures S13, S14, and S15 and Tables S3 and S4.

**3.4. High Temperature Structures.** The unit-cell parameters evolution with temperature was determined for selected samples using variable temperature X-ray or neutron powder diffraction (Figures 9, S17, and S22b). All compounds exhibit essentially linear thermal expansion for the longest cell axis ( $a$  for the  $C2$  materials,  $c$  for  $P2/c$ , red in Figure 9) up to  $700^\circ\text{C}$  and nonlinear behavior below  $\sim 300^\circ\text{C}$  for the axis parallel to the  $\text{Ga}_2\text{O}_7$  chains ( $c$  for  $C2$ ,  $a$  for  $P2/c$ , blue). This nonlinearity is likely caused by minor  $\text{H}_2\text{O}$  loss on heating and suggests that  $\text{H}_2\text{O}$  is located between pyrogallate units (as previously suggested for  $\text{Ba}_3\text{YGa}_{1.9}\text{Zn}_{0.1}\text{O}_{7.45}$ ).<sup>16</sup> This is supported by the observation that the deviation is more extreme for the Zn-substituted compounds than for  $\text{Ba}_{1.5}\text{Sr}_{1.5}\text{YGa}_2\text{O}_{7.5}$ , due to the increased basicity of the substituent and the additional vacancies introduced. The monoclinic  $\beta$  angle for  $\text{Ba}_{1.5}\text{Sr}_{1.5}\text{YGa}_{2-x}\text{Zn}_x\text{O}_{7.5-x/2}$  materials remains  $\sim 90^\circ$  in the entire temperature range; however, for the  $\text{Sr}_3\text{YGa}_{2-x}\text{Zn}_x\text{O}_{7.5-x/2}$  materials  $\beta$  gradually increases up to  $250^\circ\text{C}$  before decreasing. In both series of compounds there is evidence of phase transitions at high temperatures: the  $\beta$  angle of  $\text{Sr}_3\text{YGa}_{0.8}\text{Zn}_{0.2}\text{O}_{7.4}$  decreases rapidly to  $90^\circ$  at  $\sim 850^\circ\text{C}$ , suggesting a monoclinic to orthorhombic phase transition, while for  $\text{Ba}_{1.5}\text{Sr}_{1.5}\text{YGa}_{2-x}\text{Zn}_x\text{O}_{7.5-x/2}$  materials the  $b$ -axis shows

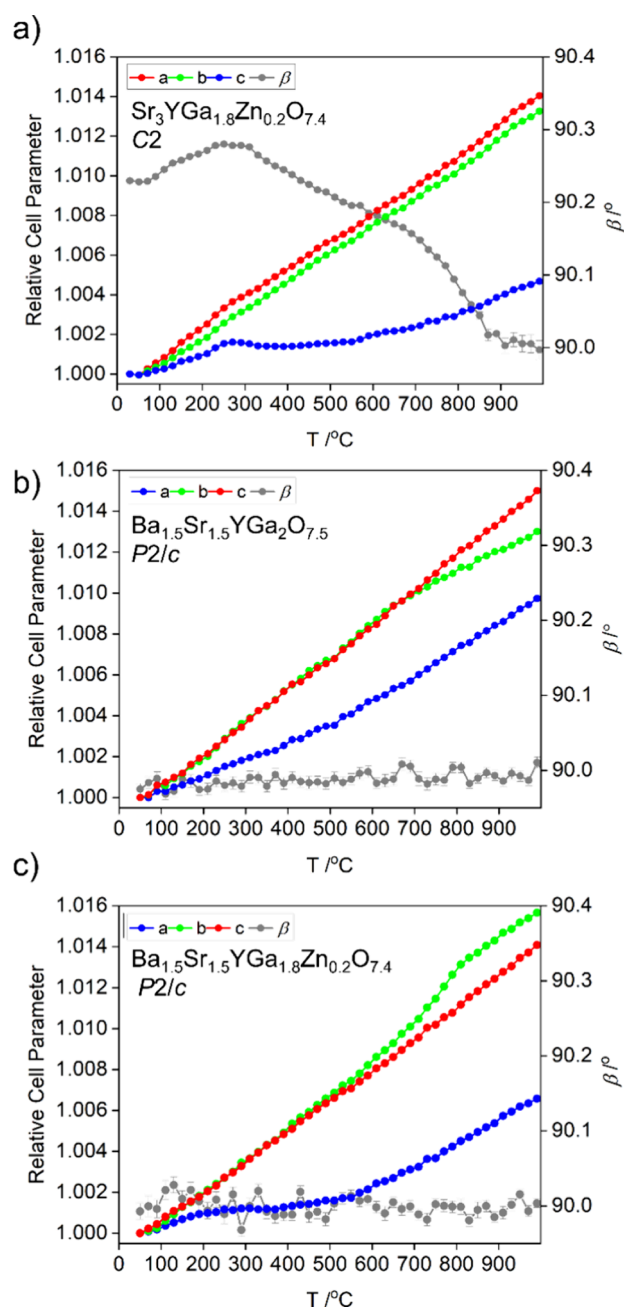


**Figure 9.** Relative unit cell axes and absolute monoclinic angle evolution as a function of temperature for (a)  $\text{Sr}_3\text{YGa}_{1.8}\text{Zn}_{0.2}\text{O}_{7.4}$ , (b)  $\text{Ba}_{1.5}\text{Sr}_{1.5}\text{YGa}_2\text{O}_{7.5}$ , (c)  $\text{Ba}_{1.5}\text{Sr}_{1.5}\text{YGa}_{1.8}\text{Zn}_{0.2}\text{O}_{7.4}$ . For cell axes error bars are smaller than data point size.

a discontinuity from around 600 °C. The temperature of this discontinuity decreases with increasing Zn-content.

A closer inspection of the variable temperature X-ray diffraction patterns of  $\text{Sr}_3\text{YGa}_{1.8}\text{Zn}_{0.2}\text{O}_{7.4}$  (Figure S16) reveals a small discontinuous jump in position for several peaks (Figure S16c). Several known structures could explain the high temperature pattern, including the *Cmcm* model discussed in the introduction or a *Pc* model similar to the high temperature structure of  $\text{Ba}_3\text{YGa}_2\text{O}_{7.5}$ , but with the *C2* type  $\text{Ga}_2\text{O}_7$  tilting. This latter model has been identified for some silicates.<sup>44</sup> Neither of these models provided a satisfactory fit to the data with several weak peaks under- or overcalculated. We therefore used the exhaustive symmetry distortion method previously

described for  $\text{Bi}_2\text{Sn}_2\text{O}_7$  to identify the best structural model.<sup>45,46</sup> A subgroup tree from the *Cmcm* parent to base child *P1* space groups was derived and it was assumed that  $\text{Ga}_2\text{O}_7$  chains were disordered. For each subgroup, the relevant distortion mode amplitudes were refined along with cell parameters. In order to rank the models, the  $R_{\text{wp}}$  for each subgroup was plotted against the number of free structural parameters (Figure S19). The high symmetry *Cmcm* model provided a poor fit to the data ( $R_{\text{wp}} \sim 8\%$ ), whereas a significantly better fit was found for space group *Ama2* ( $R_{\text{wp}} \sim 6\%$ ). The *Ama2* model gave essentially as good a fit as any other model (including a triclinic *P1* model with  $\sim 8$  times the number of free structural parameters). Sequentially fitting both the disordered *C2* and *Ama2* models to variable temperature data shows the models give equivalent fits above  $\sim 850$  °C (Figure 10a), in agreement with the temperature at which the monoclinic angle becomes 90°. A final structural model for  $\text{Sr}_3\text{YGa}_{1.8}\text{Zn}_{0.2}\text{O}_{7.4}$  obtained through a combined X-ray and neutron fit, is shown in Figure S18 (along with the fits) and Table S5.

The discontinuity in the *b*-axis expansion for  $\text{Ba}_{1.5}\text{Sr}_{1.5}\text{YGa}_2\text{O}_{7.5}$  and  $\text{Ba}_{1.5}\text{Sr}_{1.5}\text{YGa}_{1.8}\text{Zn}_{0.2}\text{O}_{7.4}$  above  $\sim 600$  °C is consistent with a phase transition from *P2/c* to *Cmcm* structures.<sup>15</sup> Refinements against neutron powder diffraction patterns with either the *P2/c* or *Cmcm* model indicate that the latter provides an equivalent fit for both materials above the transition temperature (Figures 10b,c and S21).  $\text{Ba}_{1.5}\text{Sr}_{1.5}\text{YGa}_{1.9}\text{Zn}_{0.1}\text{O}_{7.45}$  experiences a similar but less extreme deviation in the *b*-axis expansion (Figure S22b), indicating the same *P2/c* to *Cmcm* transition occurs. The larger radius of the  $\text{Zn}^{2+}$  cation likely plays a role in why the Zn-containing compounds undergo an increase in the *b*-axis, whereas  $\text{Ba}_{1.5}\text{Sr}_{1.5}\text{YGa}_2\text{O}_{7.5}$  experiences a decrease. The final Rietveld fits for  $\text{Ba}_{1.5}\text{Sr}_{1.5}\text{YGa}_2\text{O}_{7.5}$  (Figure S20 and Table S6) and  $\text{Ba}_{1.5}\text{Sr}_{1.5}\text{YGa}_{1.8}\text{Zn}_{0.2}\text{O}_{7.4}$  at 1010 °C provide excellent agreement to the data ( $R_{\text{wp}} = 2.37$  and 2.52%, respectively) using the *Cmcm* model (Figure S20c).

### 3.5. Conductivity of Zn-Substituted Compounds.

Impedance spectroscopy was performed to measure the conductivity of all materials under either air or  $\text{N}_2$  atmospheres. Complex plane plots representative of each series show a depressed semicircular response formed from two partially overlapping signals followed by a sloped electrode response that at higher temperatures gradually tapers into an arc (Figures S23 and S24). This is typical for finite Warburg type diffusion and such behavior is indicative of majority ionic conductivity.<sup>47–49</sup> Capacitances were calculated from the apex of each arc using the RC time constant relationship  $1/\omega = RC$ . The overlapping signals were separated into high and low frequency with capacitances of approximately  $10^{-12}$  and  $10^{-10}$  F indicative of bulk and grain boundary conductivity contributions.<sup>47</sup> Both components persisted down to  $\lesssim 400$  °C, at which point the data was too noisy to reliably extract resistance values. Therefore, the total conductivity ( $\sigma_b + \sigma_{\text{gb}}$ ) is reported in all cases, extracted from the intercept of the arc in the complex impedance plane. The relative density of each pellet along with firing times are given in Table S1. The conductivity of each compound is shown in Figure 11.

The conductivity of  $\text{Sr}_3\text{YGa}_2\text{O}_{7.5}$  in air shows good agreement with previous measurements.<sup>16</sup> At 1000 °C the total conductivity in the  $\text{Sr}_3\text{YGa}_{2-x}\text{Zn}_x\text{O}_{7.5-x/2}$  series increases with Zn-content, from  $\sim 0.69$  to  $5.5 \times 10^{-4}$  S  $\text{cm}^{-1}$  between  $x = 0$  and 0.2. This correlates with an increasing number of

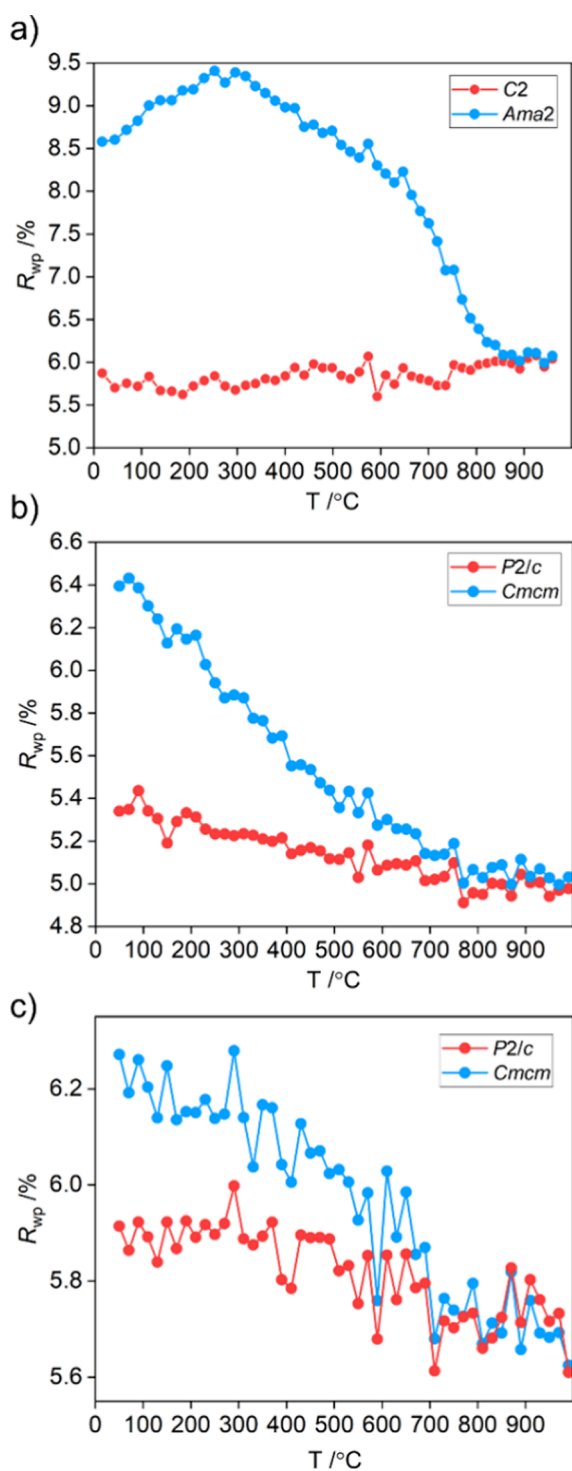


**Figure 10.**  $R_{wp}$  as a function of temperature extracted from sequential Rietveld refinements for (a)  $\text{Sr}_3\text{YGa}_{1.95}\text{Zn}_{0.05}\text{O}_{7.475}$ , (b)  $\text{Ba}_{1.5}\text{Sr}_{1.5}\text{YGa}_2\text{O}_{7.5}$ , and (c)  $\text{Ba}_{1.5}\text{Sr}_{1.5}\text{YGa}_{1.8}\text{Zn}_{0.2}\text{O}_{7.4}$ .

vacancies. The shapes of the Arrhenius plots are similar across the series and all substituted materials exhibit small changes of slope at high temperatures. This occurs for  $\text{Sr}_3\text{YGa}_{1.8}\text{Zn}_{0.2}\text{O}_{7.4}$  at 850 °C, which corresponds to the observed C2  $\leftrightarrow$  Ama2 phase transition. A plot of  $\ln(\sigma T)$  against  $1/T$  gives an activation energy of 0.93(2) eV below the phase transition temperature and 1.21(2) eV above. A slight change of slope at  $\sim 940$  °C may indicate a similar transition for both  $\text{Sr}_3\text{YGa}_{1.95}\text{Zn}_{0.05}\text{O}_{7.475}$  and  $\text{Sr}_3\text{YGa}_{1.9}\text{Zn}_{0.1}\text{O}_{7.45}$ . Activation

energies calculated from the Arrhenius plots below and above 940 °C were 0.65(1) and 0.89(1) eV for  $\text{Sr}_3\text{YGa}_{1.95}\text{Zn}_{0.05}\text{O}_{7.475}$  and 0.69(1) and 0.89(1) eV for  $\text{Sr}_3\text{YGa}_{1.9}\text{Zn}_{0.1}\text{O}_{7.45}$ .

Under wet nitrogen  $\text{Sr}_3\text{YGa}_{1.95}\text{Zn}_{0.05}\text{O}_{7.475}$  and  $\text{Sr}_3\text{YGa}_{1.8}\text{Zn}_{0.2}\text{O}_{7.4}$  show higher conductivity than in air (Figure S25). This suggests a proton component to conductivity, due to water occupying the additional vacant sites. This proton component decreases with temperature as water is lost on heating; by 1000 °C both  $x = 0.05$  and 0.20 materials show similar conductivity under air and wet nitrogen. The presence of water and its loss on heating is confirmed by TGA measurements (Figure S27). Under dry nitrogen all  $\text{Sr}_3\text{YGa}_{2-x}\text{Zn}_x\text{O}_{7.5-x/2}$  samples exhibit lower conductivities than in wet nitrogen and air, further confirming a proton contribution (Figure 11) and suggesting pure oxide ion conductivity dominates. A proton transport number,  $t_H$ , was approximated for each compound from the conductivity in wet and dry atmospheres,  $\sigma_{wet}$  and  $\sigma_{dry}$ , using

$$t_H = \frac{\sigma_{wet} - \sigma_{dry}}{\sigma_{wet}}$$

assuming dominant ionic contributions at all temperatures. At 600 °C approximately 60% of conductivity is proton-based, decreasing to around half at 1000 °C (Table S7).  $\text{Sr}_3\text{YGa}_{1.8}\text{Zn}_{0.2}\text{O}_{7.4}$  retains a larger proton component at the higher temperature consistent with the increased basicity of Zn. Proton conductivity has been demonstrated in several materials above 800 °C.<sup>50–54</sup> For perovskite barium zirconate-based materials, the proton contribution at these temperatures is often small, but it can be as high as 60%, as for  $\text{BaIn}_{0.75}\text{Zr}_{0.25}\text{O}_{2.625}$ , which exhibits a similar overall conductivity to  $\text{Sr}_3\text{YGa}_{1.8}\text{Zn}_{0.2}\text{O}_{7.4}$ .<sup>53</sup>

For the  $\text{Ba}_{1.5}\text{Sr}_{1.5}\text{YGa}_{2-x}\text{O}_{7.5-x/2}$  series overall conductivity in air increases from  $\sim 0.67$  to  $\sim 2.5 \times 10^{-4}$  S  $\text{cm}^{-1}$  between  $x = 0$  and  $x = 0.1$  at 1000 °C (Figure 11). The higher doped  $x = 0.2$  material has around half the conductivity of  $x = 0.1$  at the same temperature. Below 720 °C  $x = 0.2$  has a lower conductivity than the unsubstituted material, suggesting that charge carrier trapping inhibits ionic mobility. This is supported by the  $x = 0.05$  material having the highest conductivity in the series up to  $\sim 640$  °C. The Zn-substituted materials exhibit two distinct regions of conductivity, with activation energies of 0.66(1) and 1.01(4) eV, 0.72(1) and 1.03(2) eV, and 0.67(1) and 1.11(2) eV below and above  $\sim 650$  °C for  $x = 0.05, 0.1,$  and 0.2, respectively. The temperature at which this change occurs approximately coincides with the P2/c to Cmcm phase transition discussed above.  $\text{Ba}_{1.5}\text{Sr}_{1.5}\text{YGa}_2\text{O}_{7.5}$  is known to have a substantial proton component to conductivity up to  $\sim 900$  °C, therefore it is likely that the lower activation energies at low temperature represent proton mobility. This is supported by measurements on  $\text{Ba}_{1.5}\text{Sr}_{1.5}\text{YGa}_{1.9}\text{Zn}_{0.1}\text{O}_{7.45}$  (Figure S26) which show an increase and decrease in conductivity under wet and dry  $\text{N}_2$ , respectively. This suggests dominant oxide ion conductivity in dry conditions and mixed ionic conductivity in humidified conditions. A proton transport number (Table S7) calculated at 600 °C ( $\sim 0.96$ ) indicates that the majority of conductivity is proton based. Although a small p-type electronic contribution cannot be ruled out, TGA measurements on  $\text{Ba}_{1.5}\text{Sr}_{1.5}\text{YGa}_{1.9}\text{Zn}_{0.1}\text{O}_{7.45}$  confirm water retention up to  $\sim 800$  °C (Figure S27), further supporting the high-temperature proton component to conductivity.<sup>55–58</sup>

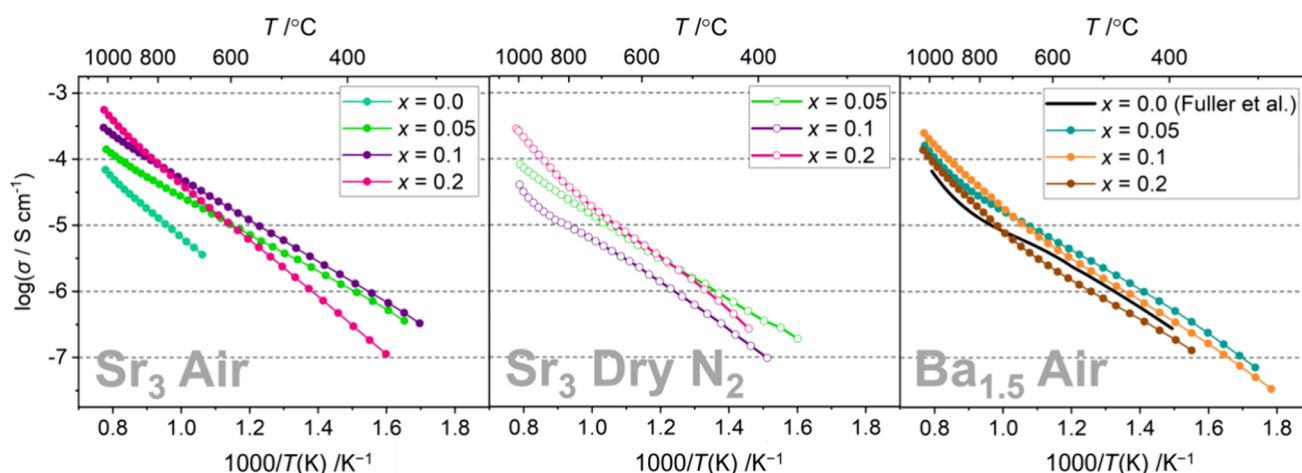


**Figure 11.** Conductivity in air (filled points) and dry  $N_2$  (empty points) of  $Sr_3YGa_{2-x}Zn_xO_{7.5-x/2}$  and  $Ba_{1.5}Sr_{1.5}YGa_{2-x}Zn_xO_{7.5-x/2}$ .

**3.6. Implications of Substitutional Chemistry.** Both AIMD simulations and diffraction studies indicate the importance of the facile reorientation of pyrogallate units during ionic migration. The effect of Zn substitution in these subunits can help rationalize the changes in ionic conductivity beyond the simple argument of increasing the number of vacancies. From the low- and high-temperature structures of  $Sr_3YGa_{1.8}Zn_{0.2}O_{7.4}$  and  $Ba_{1.5}Sr_{1.5}YGa_{1.8}Zn_{0.2}O_{7.4}$ , it is clear that the introduction of  $Zn^{2+}$  leads to the reorientation of a number of  $Td_2O_7$  groups. The fact that these polyhedra tilt in the  $ac$  plane (shown by the positions of the O8a/b and O1a sites in Figure 6), supports the diffusion pathway identified in the AIMD simulations. We can imagine that the larger non-O-linked Ga–Ga distance between separate pyrogallate units in unsubstituted  $Sr_3YGa_2O_{7.5}$  ( $\sim 4.18$  Å for Ga– $V_O$ –Ga vs  $\sim 3.68$  Å for Ga–O–Ga) results in a high energy barrier to the formation of new units. Increasing  $Zn^{2+}$  substitution systematically decreases this distance across the  $Sr_3YGa_{2-x}Zn_xO_{7.5-x/2}$  series (Figure 12). Simultaneously, the bonded Ga–Ga distance increases slightly. The shrinking of the nonbonded distance will lower the energy barrier to oxygen exchange between  $Ga_2O_7$  units, making it more facile. Furthermore, Zn–O bonds are slightly more ionic than Ga–O (electronegativity

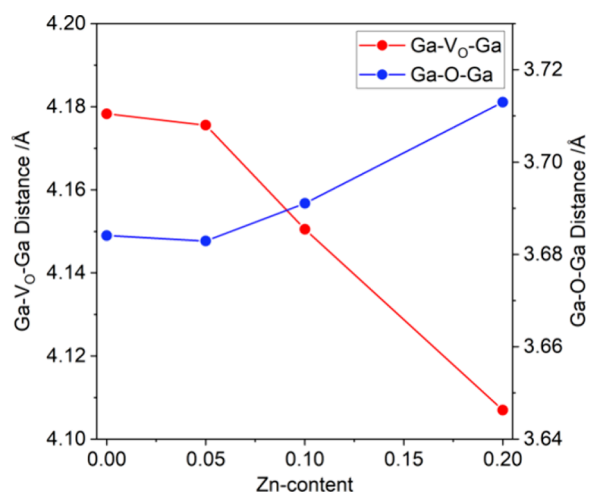


**Figure 12.** Nonbonded and bonded Ga–Ga distances with increasing Zn content in the series  $Sr_3YGa_{2-x}Zn_xO_{7.5-x/2}$ . Errors are on the order of size of data points.

difference: Zn–O = 1.79, Ga–O = 1.63) and  $Zn^{2+}$  is less polarizing, which could facilitate the formation and breakup of  $Td_2O_7$  units in Zn-containing materials relative to the Zn-free parent phases.

In both series, the activation energy calculated from impedance increases with Zn-content. Sample densities were comparable across the series, suggesting a composition-specific factor causing the increase. Given the one-dimensional diffusion pathway, a steric factor originating from the size of the  $Zn^{2+}$  cation ( $r_{ion} \sim 0.60$  Å compared to 0.43 Å for  $Ga^{3+}$ ) may inhibit long-range oxide ion diffusion at lower temperatures. This could explain the lower total conductivity of  $Sr_3YGa_{1.8}Zn_{0.2}O_{7.4}$  below 600 °C in comparison with other  $Sr_3YGa_{2-x}Zn_xO_{7.5-x/2}$  phases, and why proton conductivity (a smaller charge carrier) dominates at lower temperatures.

#### 4. CONCLUSIONS

We have used a combination of computational and experimental techniques to investigate the mechanism of ionic conductivity in  $A_3OhTd_2O_{7.5}$  materials. AIMD simulations of  $Sr_3YGa_2O_{7.5}$  indicate a one-dimensional pathway of oxide ion migration involving a series of jumps between adjacent pyrogallate units parallel to the  $c$ -axis. Both the bridging and terminal oxygen atoms are highly mobile, hence facilitating the breaking and formation of new pyrogallate groups. A high degree of anisotropy of ionic diffusion was observed from visualization of the atomic displacement clouds as well as the calculated mean square displacements. The simulations also revealed localized polyhedral tilting dynamics responsible for the structural phase transitions observed at high temperatures.

The results of our simulations were used to inform synthetic work to increase the ionic conductivity of  $Sr_3YGa_2O_{7.5}$  and  $Ba_{1.5}Sr_{1.5}YGa_2O_{7.5}$  through chemical modifications. X-ray and neutron powder diffraction studies show the Zn-substituted materials in both series adopt the room temperature structures of their parent phases (C2 and P2/c, respectively), with additional disorder introduced through the pivoting of  $Ga_2O_7$  units as a result of the partial substitution of the larger  $Zn^{2+}$  cation at tetrahedral sites and the formation of additional oxygen vacancies.  $Sr_3YGa_{2-x}Zn_xO_{7.5-x/2}$  compounds with  $x \leq 0.1$  retain the C2 parent structure up to 1000 °C, while  $Sr_3YGa_{1.8}Zn_{0.2}O_{7.4}$  undergoes a phase transition to an orthorhombic *Ama2* structure at 850 °C. All

$\text{Ba}_{1.5}\text{Sr}_{1.5}\text{YGa}_{2-x}\text{O}_{7.5-x/2}$  compounds undergo phase transitions to the *Cmcm* structure at high temperatures, with the transition temperature decreasing with Zn-content.

Total conductivity was investigated using impedance spectroscopy. Higher Zn-content increases the total conductivity at 1000 °C across the  $\text{Sr}_3\text{YGa}_{2-x}\text{Zn}_x\text{O}_{7.5-x/2}$  series. The maximum observed conductivity of  $5.5 \times 10^{-4} \text{ S cm}^{-1}$  is an order-of-magnitude increase over the parent phase. Measurements under different atmospheres indicate a substantial nonoxide ion component to conductivity, with proton conductivity dominating at lower temperatures. Zn-substitution also increases conductivity in the  $\text{Ba}_{1.5}\text{Sr}_{1.5}\text{YGa}_{2-x}\text{O}_{7.5-x/2}$  series up to  $x = 0.1$ .

The combination of experimental and computational work presented here can be used to propose chemical modifications to further improve the properties. For example, aliovalent substitution at the tetrahedral site with smaller cations could reduce the steric factors inhibiting long-range ionic diffusion at lower temperatures. The growth of high-quality large single crystals would enable impedance measurements on oriented samples, allowing experimental verification and exploitation of anisotropic conductivity revealed by the AIMD simulations.

## ■ ASSOCIATED CONTENT

### SI Supporting Information

The Supporting Information is available free of charge at <https://pubs.acs.org/doi/10.1021/acs.chemmater.5c00426>.

Additional AIMD simulations details; diffraction patterns (XRD and NPD) and unit cell parameters of synthesized compounds along with detailed crystallographic information for all compositions; Rietveld refinement agreement factors for 67 subgroups; variable temperature diffraction patterns; Nyquist plots and Arrhenius curves from impedance measurements; TGA data and proton transport numbers for representative compositions; and animation of polyhedral tilting in AIMD simulations (ISOVIZ) (PDF)

Dynamics ISOVIZ (TXT)

## ■ AUTHOR INFORMATION

### Corresponding Authors

John S. O. Evans – Department of Chemistry, Durham University, Durham DH1 3LE, U.K.; [orcid.org/0000-0001-6305-6341](https://orcid.org/0000-0001-6305-6341); Email: [john.evans@durham.ac.uk](mailto:john.evans@durham.ac.uk)

Ivana Radosavljevic Evans – Department of Chemistry, Durham University, Durham DH1 3LE, U.K.; [orcid.org/0000-0002-0325-7229](https://orcid.org/0000-0002-0325-7229); Email: [ivana.radosavljevic@durham.ac.uk](mailto:ivana.radosavljevic@durham.ac.uk)

### Authors

Oliver J. Wagstaff – Department of Chemistry, Durham University, Durham DH1 3LE, U.K.; [orcid.org/0009-0008-1719-1436](https://orcid.org/0009-0008-1719-1436)

Maxim Avdeev – Australian Centre for Neutron Scattering, Australian Nuclear Science and Technology Organisation, Menai, NSW 2234, Australia; School of Chemistry, The University of Sydney, Sydney, NSW 2006, Australia; [orcid.org/0000-0003-2366-5809](https://orcid.org/0000-0003-2366-5809)

Stewart J. Clark – Department of Physics, Durham University, Durham DH1 3LE, U.K.

Complete contact information is available at:

<https://pubs.acs.org/doi/10.1021/acs.chemmater.5c00426>

## Author Contributions

The manuscript was written through contributions of all authors. All authors have given approval to the final version of the manuscript.

## Funding

The authors thank Durham University for a Durham Doctoral (DDS) Scholarship for OJW. IRE and JSOE thank Durham University for research leave during which this article was written.

## Notes

The authors declare no competing financial interest.

## ■ ACKNOWLEDGMENTS

We thank Dr. Dominic Fortes (ISIS) and Dr. Christopher Howard (ISIS) for help with collecting neutron diffraction data and Doug Carswell (Durham) for assistance with TGA. We also thank Durham University for usage of the HAMILTON supercomputer through the HPC Service.

## ■ REFERENCES

- (1) Goodenough, J. B. Oxide-Ion Conductors by Design. *Nature* **2000**, *404* (6780), 821–823.
- (2) Megía, P. J.; Vizcaíno, A. J.; Calles, J. A.; Carrero, A. Hydrogen Production Technologies: From Fossil Fuels toward Renewable Sources. A Mini Review. *Energy Fuels* **2021**, *35* (20), 16403–16415.
- (3) Dufour, A. U. Fuel Cells—a New Contributor to Stationary Power. *J. Power Sources* **1998**, *71* (1), 19–25.
- (4) Irvine, J. T. S.; Dobson, J. W. L.; Politova, T.; García Martín, S.; Shenouda, A. Co-Doping of Scandia–Zirconia Electrolytes for SOFCs. *Faraday Discuss.* **2007**, *134*, 41–49.
- (5) Pérez-Coll, D.; Sánchez-López, E.; Mather, G. C. Influence of Porosity on the Bulk and Grain-Boundary Electrical Properties of Gd-Doped Ceria. *Solid State Ionics* **2010**, *181* (21), 1033–1042.
- (6) Yang, X.; Fernández-Carrión, A. J.; Kuang, X. Oxide Ion-Conducting Materials Containing Tetrahedral Moieties: Structures and Conduction Mechanisms. *Chem. Rev.* **2023**, *123* (15), 9356–9396.
- (7) Peet, J. R.; Fuller, C. A.; Frick, B.; Zbiri, M.; Piovano, A.; Johnson, M. R.; Evans, I. R. Direct Observation of Oxide Ion Dynamics in  $\text{La}_2\text{Mo}_2\text{O}_9$  on the Nanosecond Timescale. *Chem. Mater.* **2017**, *29* (7), 3020–3028.
- (8) Evans, I. R.; Howard, J. A. K.; Evans, J. S. O. The Crystal Structure of  $\alpha\text{-La}_2\text{Mo}_2\text{O}_9$  and the Structural Origin of the Oxide Ion Migration Pathway. *Chem. Mater.* **2005**, *17* (16), 4074–4077.
- (9) Kuang, X.; Green, M. A.; Niu, H.; Zajdel, P.; Dickinson, C.; Claridge, J. B.; Jantsky, L.; Rosseinsky, M. J. Interstitial Oxide Ion Conductivity in the Layered Tetrahedral Network Melilite Structure. *Nat. Mater.* **2008**, *7*, 498–504.
- (10) Didier, C.; Claridge, J.; Rosseinsky, M. Crystal Structure of Brownmillerite  $\text{Ba}_2\text{InGaO}_5$ . *J. Solid State Chem.* **2014**, *218*, 38–43.
- (11) Goodenough, J. B.; Ruiz-Diaz, J. E.; Zhen, Y. S. Oxide-Ion Conduction in  $\text{Ba}_2\text{In}_2\text{O}_5$  and  $\text{Ba}_3\text{In}_2\text{MO}_8$  ( $M = \text{Ce}, \text{Hf}, \text{or Zr}$ ). *Solid State Ionics* **1990**, *44* (1), 21–31.
- (12) Kuang, X.; Payne, J. L.; Johnson, M. R.; Radosavljevic Evans, I. Remarkably High Oxide Ion Conductivity at Low Temperature in an Ordered Fluorite-Type Superstructure. *Angew. Chem., Int. Ed.* **2012**, *51* (3), 690–694.
- (13) Peet, J. R.; Fuller, C. A.; Frick, B.; Koza, M. M.; Johnson, M. R.; Piovano, A.; Evans, I. R. Insight into Design of Improved Oxide Ion Conductors: Dynamics and Conduction Mechanisms in the  $\text{Bi}_{0.913}\text{V}_{0.087}\text{O}_{1.587}$  Solid Electrolyte. *J. Am. Chem. Soc.* **2019**, *141* (25), 9989–9997.
- (14) Chambers, M. S.; McCombie, K. S.; Auckett, J. E.; McLaughlin, A. C.; Irvine, J. T. S.; Chater, P. A.; Evans, J. S. O.; Evans, I. R. Hexagonal Perovskite Related Oxide Ion Conductor  $\text{Ba}_3\text{NbMoO}_{8.5}$ :

Phase Transition, Temperature Evolution of the Local Structure and Properties. *J. Mater. Chem. A* **2019**, *7* (44), 25503–25510.

(15) Fuller, C. A.; Blom, D. A.; Vogt, T.; Evans, I. R.; Evans, J. S. O. Oxide Ion and Proton Conductivity in a Family of Highly Oxygen-Deficient Perovskite Derivatives. *J. Am. Chem. Soc.* **2022**, *144* (1), 615–624.

(16) Fuller, C. A.; Murrell, J. I.; Blom, D. A.; Vogt, T.; Zhang, W.; Halasyamani, P. S.; Evans, I. R.; Evans, J. S. O. Oxide Ion Conductivity, Proton Conductivity, and Phase Transitions in Perovskite-Derived  $\text{Ba}_{3-x}\text{Sr}_x\text{YGa}_2\text{O}_{7.5}$   $0 \leq x \leq 3$  Materials. *Chem. Mater.* **2022**, *34* (7), 3185–3196.

(17) Brown, A. J.; Avdeev, M.; Manjón-Sanz, A.; Brand, H. E. A.; Ling, C. D. Competing Magnetic Interactions and the Role of Unpaired 4f Electrons in Oxygen-Deficient Perovskites  $\text{Ba}_3\text{RFe}_2\text{O}_{7.5}$  ( $\text{R} = \text{Y}, \text{Dy}$ ). *Inorg. Chem.* **2023**, *62* (17), 6786–6793.

(18) Corti, L.; Iuga, D.; Claridge, J. B.; Rosseinsky, M. J.; Blanc, F. Disorder and Oxide Ion Diffusion Mechanism in  $\text{La}_{1.54}\text{Sr}_{0.46}\text{Ga}_3\text{O}_{7.27}$  Melilite from Nuclear Magnetic Resonance. *J. Am. Chem. Soc.* **2023**, *145*, 21817.

(19) Wei, X.; Li, X.; Wang, X.; Liu, J.; Luo, Z.; Deng, S.; He, L.; Sun, J.; Kuang, X.; Xing, X. Oxygen Vacancy Migration in  $\text{Ca}_2\text{Ga}_{2+x}\text{Ge}_{1-x}\text{O}_{7-0.5x}$  Melilite. *ACS Appl. Energy Mater.* **2023**, *6* (7), 3986–3995.

(20) Abakumov, A. M.; Shpanchenko, R. V.; Lebedev, O. I.; Van Tendeloo, G.; Amelinckx, S.; Antipov, E. V. The Phase Transitions and Crystal Structures of  $\text{Ba}_3\text{RM}_2\text{O}_{7.5}$  Complex Oxides ( $\text{R} = \text{Rare-Earth Elements}, \text{M} = \text{Al}, \text{Ga}$ ). *Acta Crystallogr. A Found Crystallogr.* **1999**, *55* (5), 828–839.

(21) Tamazyan, R. A. Crystal Structure and Twinning of  $\text{Na}_2\text{B}_6[\text{Si}_2\text{O}_7][\text{SiO}_4]_2$ . *Soviet Phys. Crystallogr.* **1987**, *32* (4), 519.

(22) Wang, C. H.; Guo, D. F.; Li, Z. F.; Wang, X. M.; Lin, J. H.; Zeng, Z. Z.; Jing, X. P. Crystal Structure of  $\text{Sr}_6\text{Y}_2\text{Al}_4\text{O}_{15}$ : XRD Refinements and First-Principle Calculations. *J. Solid State Chem.* **2012**, *192*, 195–200.

(23) Coelho, A. A.; Evans, J.; Evans, I.; Kern, A.; Parsons, S. The TOPAS Symbolic Computation System. *Powder Diffr.* **2011**, *26* (S1), S22–S25.

(24) Dinnebier, R. E.; Leineweber, A.; Evans, J. S. O. *Rietveld Refinement: Practical Powder Diffraction Pattern Analysis Using TOPAS; De Gruyter STEM*, 2018; Vol. 1. .

(25) Rietveld, H. M. A Profile Refinement Method for Nuclear and Magnetic Structures. *J. Appl. Crystallogr.* **1969**, *2* (2), 65–71.

(26) ISIS HRPD Technical Information. <https://www.isis.stfc.ac.uk/Pages/Hrpd-technical-information.aspx> (accessed 2024-03-19).

(27) Liss, K.-D.; Hunter, B.; Hagen, M.; Noakes, T.; Kennedy, S. Echidna—the New High-Resolution Powder Diffractometer Being Built at OPAL. *Physica B: Condensed Matter* **2006**, *385–386*, 1010–1012.

(28) Segall, M. D.; Lindan, P. J. D.; Probert, M. J.; Pickard, C. J.; Hasnip, P. J.; Clark, S. J.; Payne, M. C. First-Principles Simulation: Ideas, Illustrations and the CASTEP Code. *J. Phys.: Condens. Matter* **2002**, *14* (11), 2717.

(29) Goret, G.; Aoun, B.; Pellegrini, E. MDANSE: An Interactive Analysis Environment for Molecular Dynamics Simulations. *J. Chem. Inf. Model.* **2017**, *57* (1), 1–5.

(30) Momma, K.; Izumi, F. VESTA: A Three-Dimensional Visualization System for Electronic and Structural Analysis. *J. Appl. Crystallogr.* **2008**, *41* (3), 653–658.

(31) Santibáñez-Mendieta, A. B.; Didier, C.; Inglis, K. K.; Corkett, A. J.; Pitcher, M. J.; Zanella, M.; Shin, J. F.; Daniels, L. M.; Rakhmatullin, A.; Li, M.; Dyer, M. S.; Claridge, J. B.; Blanc, F.; Rosseinsky, M. J.  $\text{La}_3\text{Li}_3\text{W}_2\text{O}_{12}$ : Ionic Diffusion in a Perovskite with Lithium on Both A- and B-Sites. *Chem. Mater.* **2016**, *28* (21), 7833–7851.

(32) Perrichon, A.; Koza, M. M.; Evenson, Z.; Frick, B.; Demmel, F.; Fouquet, P.; Karlsson, M. Proton Diffusion Mechanism in Hydrated Barium Indate Oxides. *Chem. Mater.* **2023**, *35* (17), 6713–6725.

(33) Schwaighofer, B.; Gonzalez, M. A.; Evans, I. R. Computational Insights into Dion–Jacobson Type Oxide Ion Conductors. *J. Phys. Chem. C* **2024**, *128* (22), 8894–8899.

(34) Schwaighofer, B.; Gonzalez, M. A.; Appel, M.; Koza, M. M.; Evans, I. R. Oxide Ion Mobility in V- and P-Doped  $\text{Bi}_2\text{O}_3$ -Based Solid Electrolytes: Combining Quasielastic Neutron Scattering with Ab Initio Molecular Dynamics. *Chem. Mater.* **2023**, *35* (3), 1125–1133.

(35) Gómez-Toledo, M.; Arroyo-de Dompablo, E. M. Ab Initio Investigation of Oxygen Ion Diffusion in the Layered Perovskite System  $\text{YSr}_2\text{Cu}_2\text{FeO}_{7+\delta}$  ( $0 < \delta < 1$ ). *Applied Sciences* **2024**, *14* (15), 6586.

(36) Wiedemann, D. CalcOPP: A Program for the Calculation of One-Particle Potentials (OPPs). *Zeitschrift für Kristallographie - Crystalline Materials* **2022**, *237* (4–5), 85–92.

(37) Simura, R.; Suzuki, Y.; Yamane, H. Perovskite-Related Structures of  $\text{Ba}_3\text{YAlO}_5$  and the  $\beta$  and  $\alpha$  Phases of  $\text{Ba}_6\text{Y}_2\text{Al}_4\text{O}_{15}$  Containing  $\text{AlO}_4$  Tetrahedra. *Acta Cryst. C* **2023**, *79* (11), 464–471.

(38) Kapusta, B.; Guillopé, M. Molecular Dynamics Study of the Perovskite  $\text{MgSiO}_3$  at High Temperature: Structural, Elastic and Thermodynamical Properties. *Physics of the Earth and Planetary Interiors* **1993**, *75* (4), 205–224.

(39) Sepiarsky, M.; Stachiotti, M. G.; Migoni, R. L.; Rodriguez, C. O. Dynamic Mechanisms of the Structural Phase Transitions in  $\text{KNbO}_3$ : Molecular Dynamics Simulations. *Ferroelectrics* **1999**, *234* (1), 9–27.

(40) Carignano, M. A.; Aravindh, S. A.; Roqan, I. S.; Even, J.; Katan, C. Critical Fluctuations and Anharmonicity in Lead Iodide Perovskites from Molecular Dynamics Supercell Simulations. *J. Phys. Chem. C* **2017**, *121* (38), 20729–20738.

(41) Almishal, S. S. I.; Rashwan, O. New Accurate Molecular Dynamics Potential Function to Model the Phase Transformation of Cesium Lead Triiodide Perovskite ( $\text{CsPbI}_3$ ). *RSC Adv.* **2020**, *10* (72), 44503–44511.

(42) Diaz-Lopez, M.; Shin, J. F.; Li, M.; Dyer, M. S.; Pitcher, M. J.; Claridge, J. B.; Blanc, F.; Rosseinsky, M. J. Interstitial Oxide Ion Conductivity in the Langasite Structure: Carrier Trapping by Formation of  $(\text{Ga}, \text{Ge})_2\text{O}_8$  Units in  $\text{La}_3\text{Ga}_{5-x}\text{Ge}_{1+x}\text{O}_{14+x/2}$  ( $0 < x \leq 1.5$ ). *Chem. Mater.* **2019**, *31* (15), 5742–5758.

(43) Auckett, J. E.; Milton, K. L.; Evans, I. R. Cation Distributions and Anion Disorder in  $\text{Ba}_3\text{NbMO}_{8.5}$  ( $\text{M} = \text{Mo}, \text{W}$ ) Materials: Implications for Oxide Ion Conductivity. *Chem. Mater.* **2019**, *31* (5), 1715–1719.

(44) Arroyabe, E.; Kaindl, R.; Töbrens, D. M.; Kahlenberg, V.  $\text{K}_2\text{Ca}_6\text{Si}_4\text{O}_{15}$ —Structural and Spectroscopical Studies on a Mixed Tetrahedral–Octahedral Framework. *J. Solid State Chem.* **2009**, *182* (12), 3254–3261.

(45) Lewis, J. W.; Payne, J. L.; Evans, I. R.; Stokes, H. T.; Campbell, B. J.; Evans, J. S. O. An Exhaustive Symmetry Approach to Structure Determination: Phase Transitions in  $\text{Bi}_2\text{Sn}_2\text{O}_7$ . *J. Am. Chem. Soc.* **2016**, *138* (25), 8031–8042.

(46) Campbell, B. J.; Stokes, H. T.; Tanner, D. E.; Hatch, D. M. ISODISPLACE: A Web-Based Tool for Exploring Structural Distortions. *J. Appl. Crystallogr.* **2006**, *39* (4), 607–614.

(47) Irvine, J. T. S.; Sinclair, D. C.; West, A. R. Electroceramics: Characterization by Impedance Spectroscopy. *Adv. Mater.* **1990**, *2* (3), 132–138.

(48) Fop, S.; Skakle, J. M. S.; McLaughlin, A. C.; Connor, P. A.; Irvine, J. T. S.; Smith, R. I.; Wildman, E. J. Oxide Ion Conductivity in the Hexagonal Perovskite Derivative  $\text{Ba}_3\text{MoNbO}_{8.5}$ . *J. Am. Chem. Soc.* **2016**, *138* (S1), 16764–16769.

(49) Lazanas, A. Ch.; Prodromidis, M. I. Electrochemical Impedance Spectroscopy—A Tutorial. *ACS Meas. Sci. Au* **2023**, *3* (3), 162–193.

(50) Nalini, V.; Haugsrud, R.; Norby, T. High-Temperature Proton Conductivity and Defect Structure of  $\text{TiP}_2\text{O}_7$ . *Solid State Ionics* **2010**, *181* (11), 510–516.

(51) Nalini, V.; Amezawa, K.; Xing, W.; Norby, T. High Temperature Proton Conductivity of  $\text{ZrP}_2\text{O}_7$ . *J. Electrochem. Soc.* **2010**, *157* (10), B1491.

(52) Kreuer, K. D. Proton-Conducting Oxides. *Annu. Rev. Mater. Res.* **2003**, *33* (1), 333–359.

(53) Świerczek, K.; Zając, W.; Klimkiewicz, A.; Zheng, K.; Malikova, N.; Dabrowski, B. Crystal Structure and Proton Conductivity in

Highly Oxygen-Deficient  $\text{Ba}_{1-x}\text{La}_x(\text{In,Zr,Sn})\text{O}_{3-\delta}$  Perovskites. *Solid State Ionics* **2015**, *275*, 58–61.

(54) Brown, A. J.; Wagstaff, O. J.; Evans, I. R.; Evans, J. S. O.; Mole, R. A.; Wykes, J.; Avdeev, M.; Ling, C. D. Distinct Intercalation and Conduction Behaviors within an Isostructural Series  $\text{Ba}_5\text{R}_2\text{Al}_2\text{SnO}_{13}$ . *Chem. Mater.* **2024**, *36* (17), 8188–8198.

(55) Qin, J.; Jiang, P.; Lu, G.; Wang, R.; Yang, T. Temperature-Driven Order–Disorder Structural Transition in the Oxygen Sub-Lattice and the Complex Superstructure of the High-Temperature Polymorph of  $\text{CaSrZn}_2\text{Ga}_2\text{O}_7$ . *Dalton Trans.* **2022**, *51* (48), 18549–18561.

(56) Gong, J.; Xu, L.; Zhu, W.; Xie, L.; Chen, X.; Liu, X. High-Performance Co-Free Ruddlesden–Popper-Type Perovskites by In Situ-Controlled Exsolution-Defined Nanocomposites for Protonic Ceramic Fuel Cell Cathodes. *ACS Sustainable Chem. Eng.* **2024**, *12* (9), 3757–3765.

(57) Antonova, E.; Tropin, E. Composite  $\text{LaNi}_{0.6}\text{Fe}_{0.4}\text{O}_{3-\delta}$  -  $\text{La}_{0.9}\text{Sr}_{0.1}\text{Sc}_{0.9}\text{Co}_{0.1}\text{O}_{3-\delta}$  Cathodes for Proton Conducting Solid Oxide Fuel Cells: Electrode Kinetics Study. *Ceram. Int.* **2024**, *50* (20,Part C), 40492–40499.

(58) Dong, Y.; Huang, Y.; Ding, D.; Wu, W.; Yao, X.; Li, J. Chemical and Structural Origin of Hole States in Ytria-Stabilized Zirconia. *Acta Mater.* **2021**, *203*, No. 116487.